Coastal Engineering 60 (2012) 149–166

Contents lists available at SciVerse ScienceDirect

Coastal Engineering

journal homepage: www.elsevier.com/locate/coastaleng

Experimental study of bore-driven swash hydrodynamics on impermeable rough slopes

G.A. Kikkert [a,*], T. O'Donoghue [b], D. Pokrajac [b], N. Dodd [c]

[a] Department of Civil and Environmental Engineering, School of Engineering, Hong Kong University of Science and Technology, Hong Kong
[b] School of Engineering, King's College, University of Aberdeen, Aberdeen, AB24 3UE, United Kingdom
[c] Department of Civil Engineering, Faculty of Engineering, University of Nottingham, University Park, Nottingham, NG7 2RD, United Kingdom

ARTICLE INFO

Article history:
Received 6 April 2011
Received in revised form 28 September 2011
Accepted 28 September 2011
Available online 27 October 2011

Keywords:
Dam-break
Swash
Laboratory experiments
Bore
Turbulence
Shear stress

ABSTRACT

A detailed experimental investigation of the hydrodynamics of large-scale, bore-driven swash on impermeable, rough beach slopes is described. The experiments were carried out on 1:10 impermeable, rough slopes with three different surface roughnesses based on 1.3 mm sand, 5.4 mm gravel and 8.4 mm gravel. The large-scale discrete swash event was produced by the collapse of a dambreak-generated bore on the beach. Simultaneous depths and velocities were measured using LIF, Laser-induced fluorescence, and PIV, particle image velocimetry, respectively, yielding better resolution of the hydrodynamics than previous studies. Depth time-series, instantaneous velocity profiles, depth-averaged velocities, instantaneous turbulent kinetic energy profiles, depth-averaged turbulent kinetic energy, Reynolds stress profiles and bed shear stresses are presented for five cross-shore measurement locations in the swash. The measurements resolve the backwash shoreline position, and the late backwash period when depths are shallow and velocities are high. The detailed data can be used to test and develop advanced numerical models for bore-driven waves on rough slopes.

1. Introduction

Swash on steep beaches is characterised by wave breaking followed by bore collapse on the beach slope. The flow velocities generated by bore collapse can be very high, up to 5 m/s according to Hughes (1992), and the corresponding run-up on the beach can extend many metres. The swash zone is therefore a highly dynamic region of the beach, complicated in hydrodynamic terms because the flow is turbulent, highly unsteady and highly non-uniform, and in morphological terms because sediment fluxes are high and vary greatly across the swash zone. While many studies of swash carried out in the field have yielded useful insights (e.g. Austin and Masselink, 2006; Hughes, 1992; Masselink and Hughes, 1998; Puleo et al., 2000) fundamental aspects of swash are arguably best studied in controlled laboratory experiments because of the complexity of the processes at work. Table 1 lists previous laboratory studies which have investigated breaking wave and bore hydrodynamics in the swash zone, focused on the detailed hydrodynamics, the turbulence and, in some cases, the bed shear stress for smooth and rough impermeable beach slopes. The majority of the studies have been carried out in small-scale laboratory wave flumes. There are two disadvantages in using small wave flumes to study bore collapse on beaches. The first is that the relatively small scale leads to substantial scale effects in relation to roughness, permeability and sediment behaviour; the second is that the magnitudes of swash depths, velocities and maximum run-up are relatively small, making it more difficult to obtain accurate measurements of the key fundamental processes. An alternative method for generating a controlled swash event in the laboratory is to generate a large-scale bore through dam-break. A deep reservoir of water is separated from a shallow body of water by a partition that can be removed at high speed. After partition removal, the released water plunges and generates a bore travelling away from the reservoir. Subsequent bore collapse on a sloping beach located downstream results in a large-scale swash event with run-up that is an order of magnitude larger than swash run-up generated by waves on a sloping beach in a typical laboratory wave flume. The large scale of the swash means that scale effects are avoided and accurate measurements of the more detailed hydrodynamics are possible. This kind of set-up was used by Yeh (1991) and more recently by Barnes et al. (2009) and O'Donoghue et al. (2010). The dam-break swash experiment belongs to a larger family of dam-break experiments, which includes, for example, dam-break induced sediment transport on horizontal beds (e.g. Zech et al., 2008), 2D dam-break hydraulics (e.g. Aureli et al., 2008) and dam-break bore travel on a downward inclining slope (e.g. Chanson, 2004).

The present paper reports new experiments designed to study the detailed hydrodynamics of large-scale bore-driven swash on impermeable, rough beach slopes. The experiments were carried out on three impermeable 1:10 slopes with different surface roughness in order to investigate the effect of roughness on the hydrodynamics. The experiments use a similar setup to that of O'Donoghue et al.

* Corresponding author. Tel.: +852 2358 8190.
E-mail address: kikkert@ust.hk (G.A. Kikkert).

0378-3839 © 2011 Elsevier B.V. Open access under CC BY license.
doi:10.1016/j.coastaleng.2011.09.006

Table 1
Laboratory studies investigating the hydrodynamics of breaking waves in the swash zone.

Reference	Experimental details						
	Wave generation	Slope angle	Roughness (d_{50})	Velocity meas.		Depth meas.	
				Method	No. of loc's	Method	No. of loc's
Miller (1968)	Wave flume	1:3.7, 1:5.7, 1:11.4, 1:28.6	0.52 mm, 3.7 mm	Wave gauges		Optically	
Cox et al. (2000)	Wave flume	1:35 → 1:10	6.3 mm	LDV	12	Wave gauges	28
Petti and Longo (2001)	Wave flume	1:10	30 μm	LDV	3	Wave gauges	13
Cowen et al. (2003)	Wave flume	1:20	'Smooth'	PIV	2	Wave gauges	5
Gedik et al. (2005)	Wave flume	1:5	0.35 mm (12 mm armoring)	ADV		Wave gauges	6
Shin and Cox (2006)	Wave flume	1:35 → 1:10	2.2 mm	LDV	14	Wave gauges	14
Barnes et al. (2009)	Wave flume	1:10, 1:12	'Smooth', 0.2 mm	–	–	Acoustic sensors	10
Sou et al. (2010)	Wave flume	1:20	'Smooth'	PIV	2	Optically (LIF)	2
Yeh (1991)	Dam-break	1:7.6	'Smooth'	Wave Gauges		Optically (LIF)	
Barnes et al. (2009)	Dam-break	1:10	'Smooth', 6 mm	PIV	2	Acoustic sensors	
O'Donoghue et al. (2010)	Dam-break	1:10	'Smooth', 6 mm	PIV	5	Wave gauges	23

(2010) but add substantially to the previous work by extending the range of beach roughness and by better resolution of the hydrodynamics through improved measurement methods, namely, the use of Laser-induced fluorescence (LIF) to better resolve flow depth and the use of an improved particle image velocimetry (PIV) system capable of measuring bed-normal as well as bed-parallel velocities. In addition, flow depth and velocity are measured *simultaneously* in the present study allowing a more thorough and rigorous analysis of the depth-averaged and ensemble-averaged velocities and the turbulence quantities.

The paper is structured as follows. Section 2 describes the experimental set-up and measurement methods and demonstrates the high repeatability and consistency of the measurements. Section 3 presents the experimental results: ensemble-averaged results for flow depth, shoreline position, depth-averaged velocity and velocity profiles are presented first, followed by results for turbulent kinetic energy and Reynolds stress; results for bed shear stress complete the section. The main conclusions of the study are presented in Section 4.

2. Experimental setup

2.1. Facility

The experiments were carried out using an updated version of the swash rig described by O'Donoghue et al. (2010). It consists of a water reservoir built into one end of a 20 m long, 0.9 m high and 0.45 m wide, glass-sided flume (Fig. 1). The reservoir is fronted by a gate which can be raised at high speed to produce a large plunging wave leading to a bore which propagates towards an impermeable beach located downstream. The reservoir is constructed from Perspex and has inside dimensions of 983 mm × 394 mm × 832 mm (length × width × height). The reservoir exit is streamlined to ensure a smooth transition for the flow from reservoir to flume, and the gate and seal are designed to enable the gate to be opened at high speed while forming a near watertight seal when *in situ*. A steel cable connects the gate through pulleys to a 15 kg mass suspended at an elevation of 2.5 m above the laboratory floor. When released, the mass falls freely for 2 m before tensioning the cable and raising the gate. The gate is raised to 0.8 m in approximately 0.2 s.

Experiments were conducted for three impermeable, rough beaches located downstream of the water reservoir. Each beach had slope 1:10 and was made of marine plywood with a layer of sediment glued to the surface. The plywood was bolted onto a steel frame positioned to within 1 to 2 mm tolerance of the 1:10 slope. The three sediments used were 1.3 mm sand ($d_{10}=1.00$ mm, $d_{50}=1.32$ mm and $d_{90}=1.89$ mm), 5.4 mm gravel (3.64 mm, 5.4 mm and 7.76 mm) and 8.4 mm gravel (6.46 mm, 8.41 mm and 10.4 mm) (Fig. 2).

The experiments were conducted for one initial condition only: a water depth in the reservoir (h_d) of 600 mm and a water depth in front of the gate (h_0) of 62 mm (Fig. 3). The origin of the x–z coordinate system is at the initial shoreline position, located 4.82 m from the reservoir gate; the x-axis is parallel to the beach slope and is positive shoreward; the z-axis is perpendicular to the slope. The corresponding velocity components are u and w, respectively. Measurements were triggered at the moment the gate is raised, which is defined as $t=0$.

2.2. Instrumentation

Velocities were measured using cross-correlation Particle Image Velocimetry (PIV) at one location "seaward" of the beach and at 5 cross-shore locations on the beach. Narrow slots (100–200 mm long and 5 mm wide) fitted with Perspex windows were cut into the flume floor and the plywood beach panels to enable Laser illumination of the flow for the PIV measurement. Illuminating vertically upwards from below eliminates the negative effects of free surface reflections associated with illuminating vertically downwards from above. The Laser was a New Wave Solo III double-pulsed, frequency-doubled Nd YAG Laser. Its beam was focused and spread into a light sheet through a series of spherical and cylindrical lenses. Near

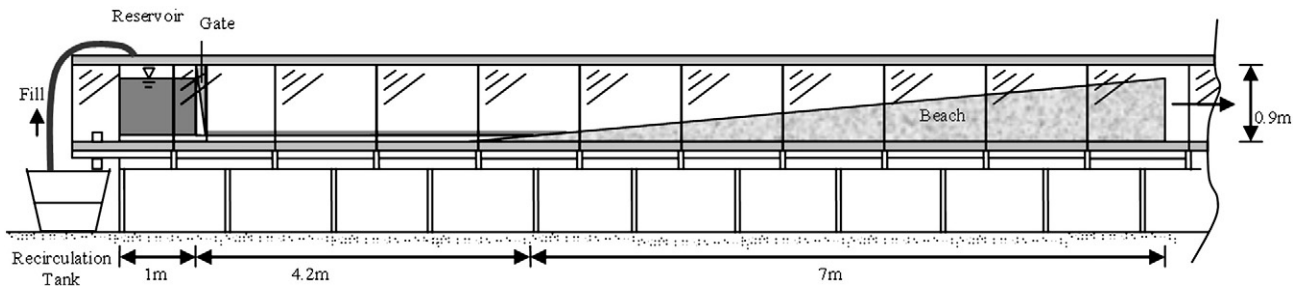

Fig. 1. The Aberdeen Swash Rig.

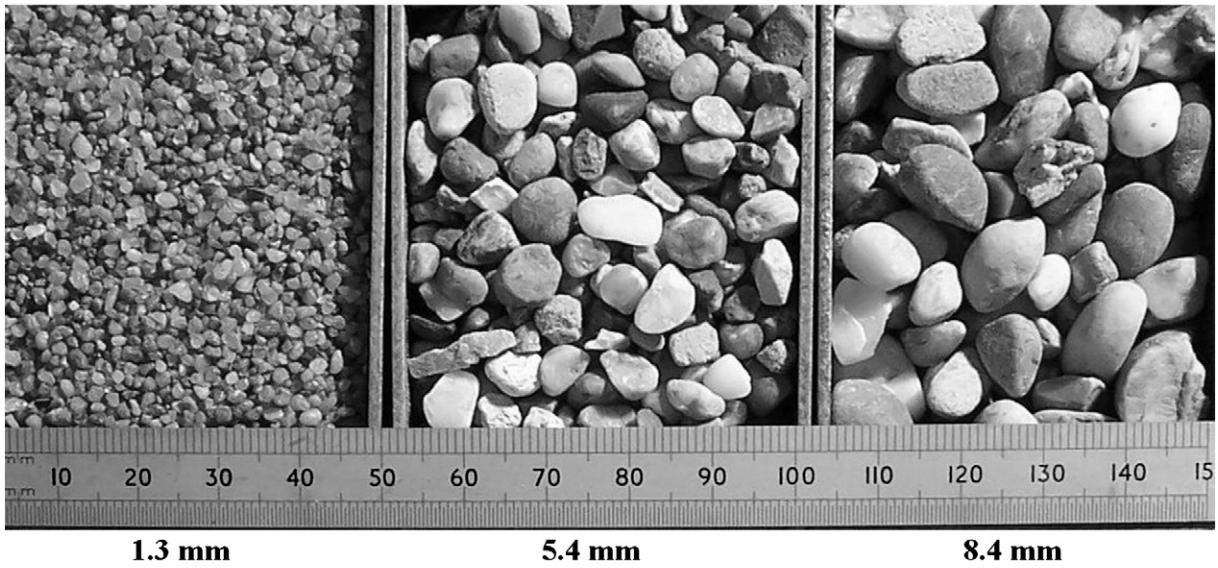

Fig. 2. Sediments used for surface roughness of the 3 beaches.

neutrally-buoyant, silver-coated, hollow glass spheres with mean diameter 15 μm were used for seeding. Velocities were measured from the beach face to the free surface. Maximum swash flow depth decreases with increasing distance from the initial shoreline, which means that a smaller flow area needs to be measured for locations further up the beach slope, with consequent increase in accuracy of the velocity measurement. The reflected Laser light from the seeding particles was captured by a Flowsense 2 M, b/w digital video camera, fitted with a 60 mm fixed focal length lens and a 532 nm narrowband green filter. The camera records two images, separated in time by 1 ms. The camera was rotated to be aligned with the 1:10 slope of the beach, so that measured velocities are bed-parallel and bed-normal. To avoid recording the reflections from the free surface when flow depths are small, the camera was rotated slightly backwards so that the camera view was below the free surface at all times (Fig. 4). The software controlling the PIV system timing, image acquisition and image analysis was DANTEC Dynamic Studio v1.45.

Flow depths were measured using Laser-induced fluorescence (LIF) (Sue et al., 2006). Fluorescent dye was added to the water, with a concentration of approximately 0.1 mg/l and illuminated by the Nd-YAG Laser. The emitted light from the fluorescent dye was recorded by a Kodak Megaplus ES1.0 b/w digital video camera fitted with a 50 mm fixed focal length lens and a Hasselblad orange filter. The camera was aligned with the 1:10 slope of the beach and rotated forwards so that the camera view was at all times above the free surface (Fig. 4).

To measure flow velocity and depth simultaneously, the PIV and LIF systems were combined into a single PIV–LIF system. The PIV software controlled the timing of the Laser pulses and the synchronisation of the PIV camera. By inserting a bnc-splitter in the connection between the timing box and the PIV camera, the timing box was also connected to the frame-grabbing board of the LIF computer. This allowed the trigger and the grabbing frequency of the LIF images to be controlled by the PIV computer and to be synchronised with the PIV camera. The combined PIV–LIF system was triggered at the moment that the gate was raised (time $t=0$). Fig. 5 shows example simultaneously-recorded PIV and LIF images. In the bottom right of both images water from the incoming bore, travelling from right to left, is visible. The similar positions of the water droplets suspended in mid-air in the two images are evidence that both images were recorded simultaneously. The images are not exactly the same because the PIV camera is rotated slightly backward and records a smaller area than the LIF camera which is rotated slightly forward. Calibrations were carried out at each position to enable the measurements to be converted from pixel-space into mm-space. A target grid, secured inside a calibration cell, was positioned on the 1:10 slope so that it coincided with the Laser Sheet. The PIV calibration image of the grid was recorded while the calibration cell was filled with water, whereas for the LIF the cell was empty.

2.3. Measurements

For each swash experiment, simultaneous flow depths (h), bed-parallel (u) and bed-normal (w) velocities were measured over a window centred at six cross-shore locations. Five were located on the beach at $x=0.072$, 0.772, 1.567, 2.377 and 3.177 m, and one seaward of the beach at $x=-1.802$ m (Fig. 3). During each experiment 140 PIV image pairs and 140 LIF images were recorded at a frequency of 13.5 Hz over approximately 10 s. For a short time immediately following bore arrival at a location, velocities could not be measured because of the relatively high percentage of entrained air in the bore front. The delay between bore arrival and the first velocity measurement was approximately 0.5 s at $x=0.072$ m and approximately 0.2 s at locations further up the slope. Individual experiments were repeated 50 times in order to determine ensemble-averaged as well as turbulent quantities. In addition to the combined PIV–LIF measurements at the 6 locations, a second set of LIF-only measurements was carried out to measure the swash lens, i.e. the instantaneous surface

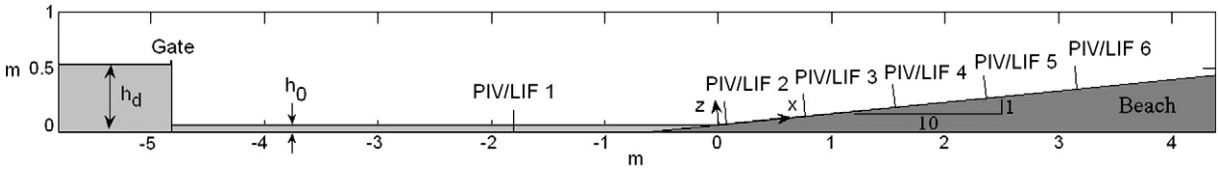

Fig. 3. Schematic of experimental setup and measurement locations.

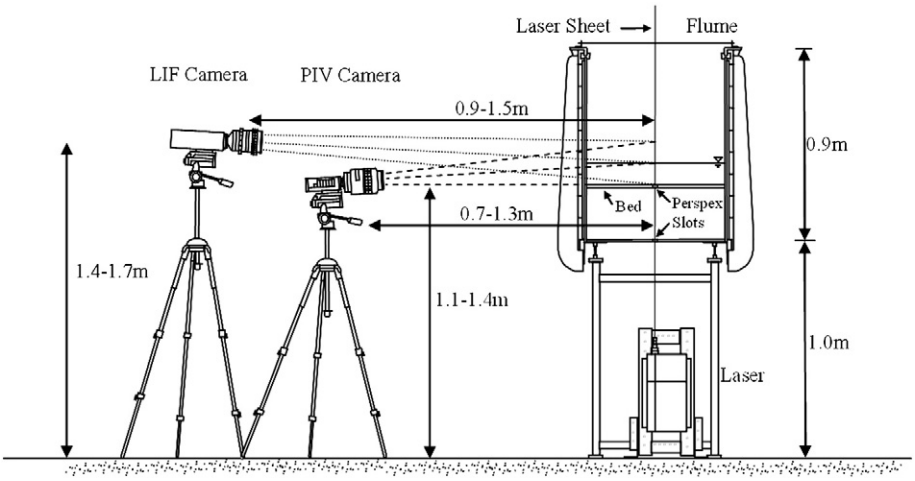

Fig. 4. PIV and LIF measurement set-up.

water profile over the whole of the swash extent. For these measurements the Laser was positioned above the flume and illuminated approximately 300 mm of the cross-shore extent of the lens. The complete lens was measured by combining measurements from approximately 16 cross-shore locations (the exact number dependent on maximum runup). For these LIF-only measurements, 140 images were recorded at a frequency of 13.5 Hz; individual experiments were repeated ten times to obtain the ensemble-averaged lens. Altogether 1380 swash runs were carried out on the three impermeable beaches.

The PIV images were analysed using an adaptive cross-correlation algorithm applied in 3 iterations, ending with 32×32 pixels. The overlap between interrogation areas was 50%, giving a 99×74 velocity vector grid with a spatial resolution between 1 and 2.5 mm, depending on the measurement area, and a random error of 5 to 15 mm/s in the instantaneous velocity components, u and w.

In the LIF images water is light and air is dark. A MATLAB-based edge detection algorithm was used to detect the interface, which was successful in determining the flow depth with an error of approximately one pixel, giving instantaneous depth measurement with a spatial resolution and random error of 0.1 to 0.3 mm. Determining depth at the longitudinal centerline of the flume was complicated by the fact that the flow is not always perfectly two-dimensional throughout the swash cycle, especially for a short time at and immediately after bore arrival at the measurement location. If the flow depth is greater on the side of the flume closest to the camera than it is in the centre of the flume (where the measurement is required), it is impossible for the camera to see the free surface at the centre. Fig. 6 shows example LIF images for a range of conditions and illustrates the algorithm successfully determining the air–water interface except on the right side of the image in Fig. 6(a), which was recorded immediately after the arrival of the bore at the measurement location.

Repeatability of swash events using the rig was excellent, which meant that measurements from many repeats of the same event could be used to produce a very detailed dataset for the swash event and to obtain turbulence measurements. Repeatability is illustrated in Fig. 7 which shows the depth time-series and the depth-averaged bed-parallel velocity time-series at $x=0.072$ m for the 1.3 mm sand-rough beach; results from the 50 individual experiments are shown together with the ensemble-averaged result. Variability in the depth is greatest just after bore arrival. There is also some variability coinciding with fluctuations in the ensemble-averaged result, caused by the plunging wave collapsing on the water in front of the gate, generating small waves that propagate with the bore towards the beach. The fluctuations, and therefore the variability in flow depth, diminish with time and increasing distance up the slope. There is very little variability in the depth-averaged velocity results up to the time of maximum backwash velocity, after which the relatively small flow depths and high velocities cause high levels of bed-generated turbulence throughout the flow column.

Note that, unlike capacitance gauges which have been used in previous swash measurements, LIF enables depth measurements to be made late into the backwash when depths are very small and velocities are high. For example, for the 1.3 mm sand-rough beach measurements were possible down to 1 mm flow depth. This advantage, combined with the high-quality PIV camera, made it possible to measure backwash velocities for flow depths down to approximately

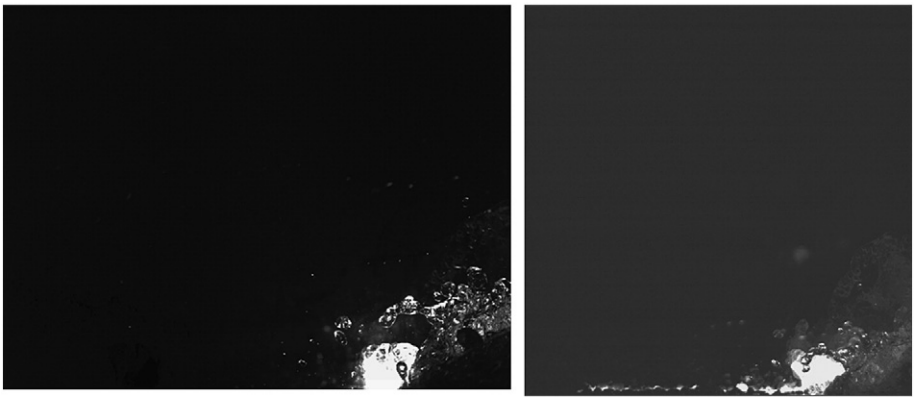

Fig. 5. Simultaneously recorded PIV (left) and LIF (right) images.

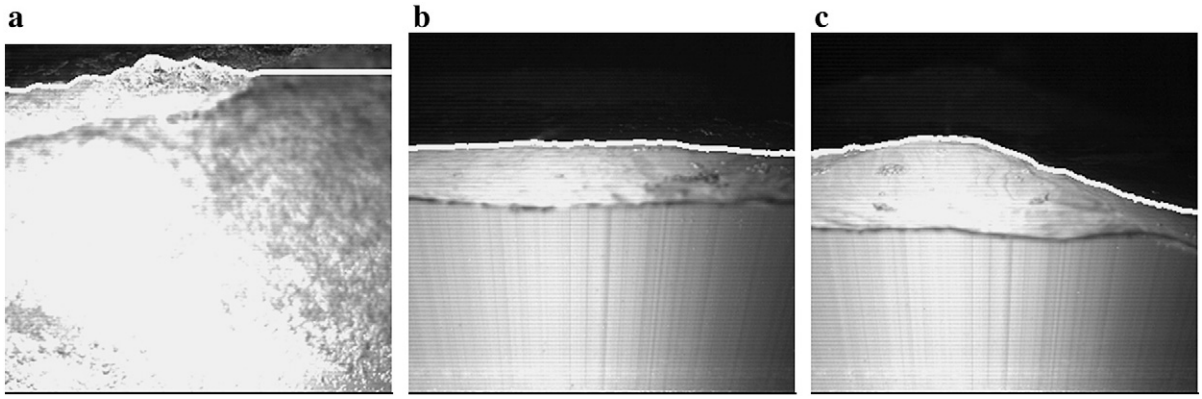

Fig. 6. Example LIF images with superimposed results from the free surface detection algorithm (white line).

5 mm. Much more of the backwash is therefore captured by the present measurements compared to O'Donoghue et al. (2010), whose backwash measurements were limited to h>15 mm. In addition, because flow depth and velocity are measured *simultaneously* in the present study, and include bed-normal velocities (absent from O'Donoghue et al. (2010)), a more thorough and rigorous analysis can be made to determine the depth-averaged and ensemble-averaged velocities and the turbulence quantities compared to previous studies.

A measure of the data consistency was obtained by comparing the ensemble-averaged flow rate per unit width, q, determined from the combined PIV–LIF measurements via

$$q(x,t) = \int_0^{\bar{h}(x,t)} \langle \bar{u} \rangle (x,t) dz \tag{1}$$

with q determined from the LIF swash lens measurement via

$$q(x,t) = \frac{1}{\Delta t}\left[\int_x^{x_s(t+\Delta t/2)} \bar{h}\,(x, t+\Delta t/2)\; dx - \int_x^{x_s(t-\Delta t/2)} \bar{h}\,(x, t-\Delta t/2) dx \right] \tag{2}$$

where $\langle \bar{u} \rangle$ is ensemble-averaged, depth-averaged bed-parallel velocity (overbar denotes ensemble-average and angled brackets denote depth-average), $\bar{h}$ is ensemble-averaged depth and x_s is shoreline position. Example comparisons of results from the two methods are shown in Fig. 8; the good agreement seen was typical of all such comparisons.

3. Results

3.1. Swash depth

Time series of ensemble-averaged flow depth, $\bar{h}$, are presented in Fig. 9 for all six measurement locations on the three beaches. The general behaviour of the flow depth seen in Fig. 9 is similar to that described by previous researchers for swash depths measured in the field (e.g. Hughes and Baldock, 2004; Hughes et al., 1997; Masselink and Hughes, 1998) and in the laboratory (Barnes et al., 2009; Cowen et al., 2003; O'Donoghue et al., 2010). At the most seaward measurement location, $x = -1.802$ m, the time series of ensemble-averaged depth for the three beaches are initially in good agreement, reflecting the repeatability of the dam-break-generated bore. Later on, especially after the flow reversal, the results for the 1.3 mm sand-rough beach lag slightly behind the other two. This is a consequence of the greater volume of water that passed the initial shoreline location during the uprush for the 1.3 mm sand-rough beach, resulting in a greater maximum runup and later flow reversal. As mentioned earlier, the depth time series show small periodic fluctuations which result from the wave plunging. These fluctuations are

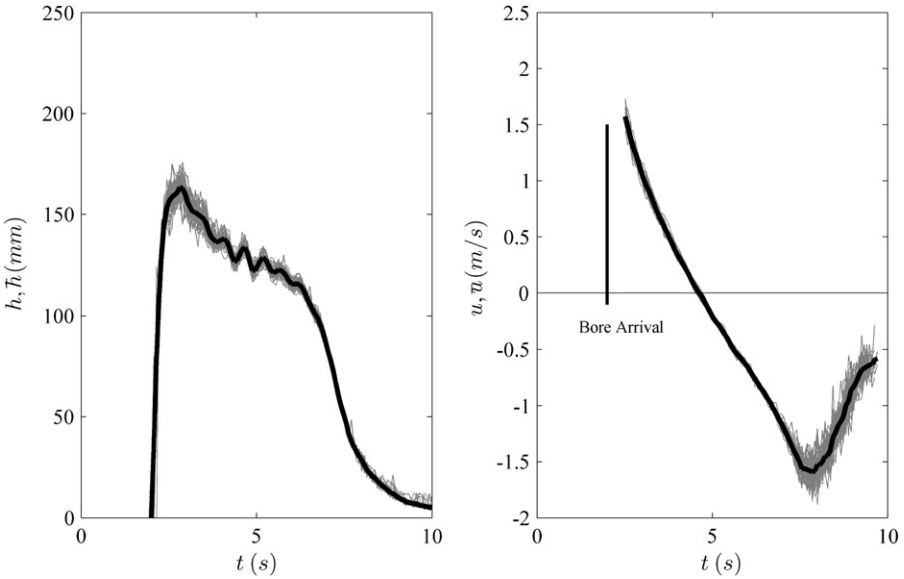

Fig. 7. Depth time-series and depth-averaged bed-parallel velocity time-series at $x = 0.072$ m for the 1.3 mm sand-rough beach; results from 50 individual events (grey) and ensemble-averaged result (black).

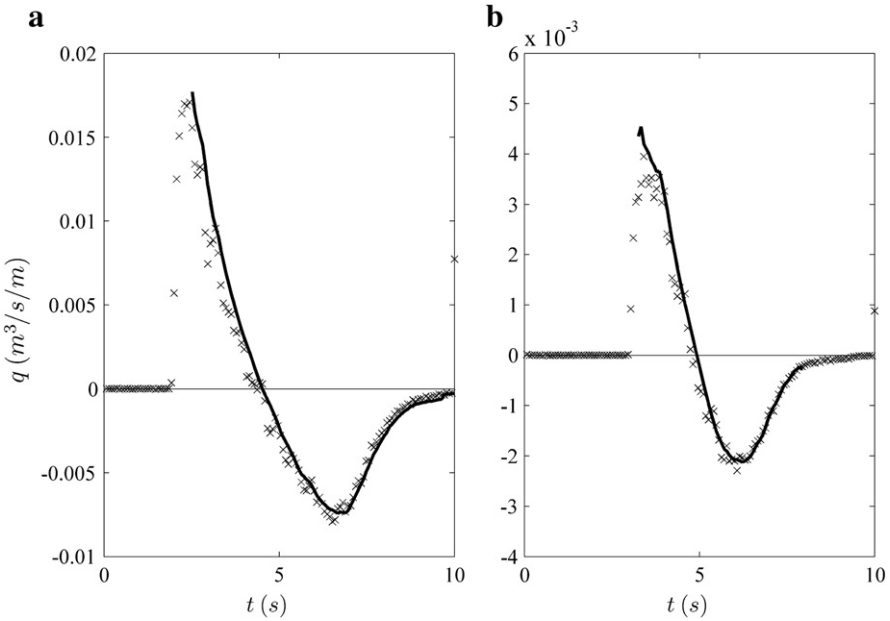

Fig. 8. Flow rate per unit width determined from LIF swash lens measurements (x) and from combined PIV–LIF velocity and depth measurements (solid lines) for (a) $x = 0.072$ m and (b) $x = 2.377$ m on the 5.4 mm gravel-rough beach.

largest at $x = -1.802$ m, diminish very quickly on the lower end of the slope, and all but disappear further up the slope. For all locations, the flow depth rapidly increases after bore arrival. At the lowest locations on the beach ($x = 0.072$ m and $x = 0.772$ m), maximum depth is followed by a period of slowly-decreasing depth, which lasts approximately 3 s for $x = 0.072$ m and approximately 2 s for $x = 0.772$ m. Further up the slope the depth decays rapidly immediately after maximum depth. The rate of decreasing depth increases during the backwash until very late in the backwash when the depths have become small. The effects of different beach roughness are better visible at locations higher up the slope, where the greater differences in depth reflect the greater differences in the volume of water flowing passed, caused by the difference in roughness.

An alternative perspective on the swash depths is shown in Fig. 10, which presents the swash lenses measured at nine times within the swash cycle for the 1.3 mm sand-rough and the 8.4 mm gravel-rough beaches. The corresponding lenses for the 5.4 mm gravel-rough beach are not shown because these lie very close to those of the 8.4 mm gravel-rough beach. The differences between the measured lenses are rather small for most of the uprush and only start to become significant as the time of maximum run-up is approached when swash on the 1.3 mm sand-rough beach reaches further up the slope than on the 8.4 mm gravel-rough beach. While differences between the uprush lenses of the two beaches are only apparent at the lens tip, differences in the backwash lenses are seen over the whole swash lens, with backwash depths for the 8.4 mm gravel-rough beach being lower than those of the 1.3 mm sand-rough beach. This is because maximum volume of water on the beach is lower, resulting in a lower maximum run-up and flow reversal occurring earlier in the case of the 8.4 mm beach. These results are

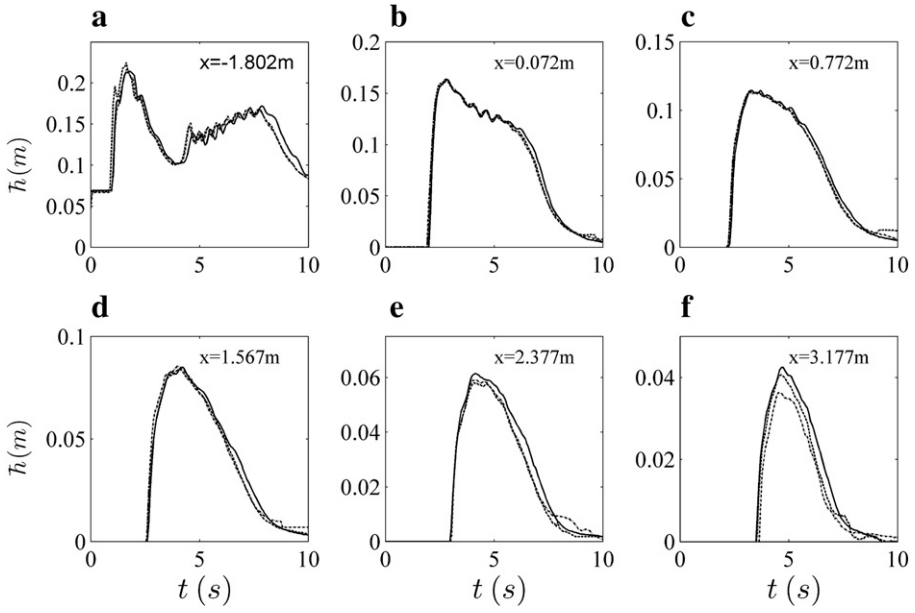

Fig. 9. Depth time-series at all six measurement locations for the 1.3 mm sand-rough (-), the 5.4 mm gravel-rough (--) and the 8.4 mm gravel-rough (-.-.) beaches.

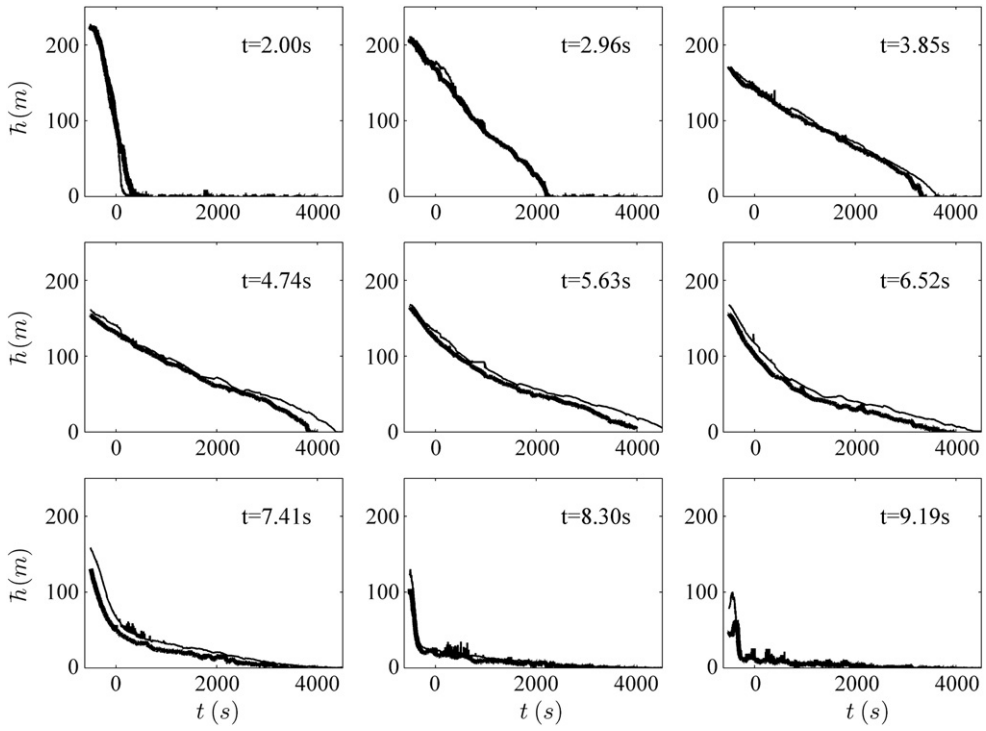

Fig. 10. Swash lenses at nine times for 1.3 mm sand-rough (thin line) and 8.4 mm gravel-rough (thick line) beaches.

consistent with the findings of O'Donoghue et al. (2010), who measured lenses on a smooth Perspex beach and a 5–6 mm gravel-rough beach.

Time-series of shoreline position obtained from the swash lenses are presented for each of the three beaches in Fig. 11. The shoreline is here defined as that location on the lens where the water depth is equal to 5 mm. 5 mm was chosen because it was the smallest depth that could be accurately measured for all three beaches. During uprush the position of the shoreline is not sensitive to the choice of water depth defining its position (O'Donoghue et al., 2010). However, in the backwash the slope of the flow profile becomes very gradual and shoreline position is then sensitive to the choice of flow depth used to define it. Following gate opening it took approximately 2 s for the bore to arrive at the initial shoreline location. The effect of roughness on the shoreline position is negligible for the first 1.5 s following bore arrival. Thereafter the higher roughness results in greater deceleration and lower maximum runup: maximum runup is 3.95 m, 4.12 m and 4.52 m for the 8.4 mm gravel-rough, 5.4 mm gravel-rough, and 1.3 mm sand-rough beach respectively. The time of maximum runup is approximately the same for the three beaches at around $t = 5.5$ s. Fig. 11 also shows the times of flow reversal (based on the ensemble-averaged depth-averaged velocity time-series, Fig. 12) at the five PIV measurement locations on the beach. There is a small difference in the flow reversal time at each position between the three beaches, with reversal occurring slightly sooner on the rougher beaches. The increasingly later time of flow reversal for locations further up the beach clearly illustrates the divergent nature of the flow and is consistent with the characteristics of the velocity obtained in the field by Masselink and Hughes (1998). Finally, the results for uprush in Fig. 11 echo those of O'Donoghue et al. (2010) for shoreline position on a smooth Perspex beach and a gravel-rough beach, but the present results for backwash go beyond those of O'Donoghue et al. (2010) who were unable to resolve the backwash shoreline position from their capacitance gauge depth measurements.

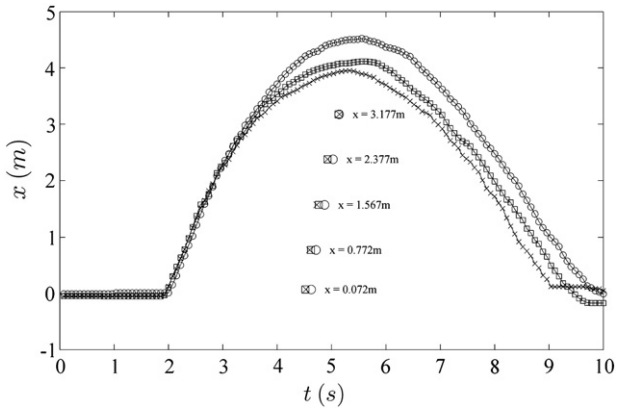

Fig. 11. Shoreline position time-series and times of flow reversal at the five measurement locations on the beach for the 1.3 mm sand-rough (o), 5.4 mm gravel-rough (□) and 8.4 mm gravel-rough (x) beaches.

3.2. Depth-averaged velocity

Time series of ensemble-averaged, depth-averaged, bed-parallel velocity, $\langle \overline{u} \rangle$ are presented in Fig. 12 for the six measurement locations and the three beaches. The measurements for the location seaward of the beach, $x = -1.802$ m, echo the depth measurements for the same location (Fig. 9): for all 3 beaches the $\langle \overline{u} \rangle$ time-series are nearly identical for the majority of the uprush period and are similar during the backwash, with $\langle \overline{u} \rangle$ time series for the 1.3 mm sand-rough beach lagging slightly behind the other two. Features of the ensemble-averaged depth-averaged time-series are in agreement with those from measurements obtained in the field (e.g. Hughes and Baldock, 2004; Masselink and Hughes, 1998; Puleo et al., 2000) and the laboratory (e.g. O'Donoghue et al., 2010). Maximum uprush velocity at a given location occurs at the time of bore arrival and the flow decelerates during uprush. Maximum values of $\langle \overline{u} \rangle$ exceed 2 m/s, which is of similar order of magnitude as high swash velocities measured in the field (Elfrink and Baldock, 2002). The longer time gap between the time of bore arrival and the first velocity

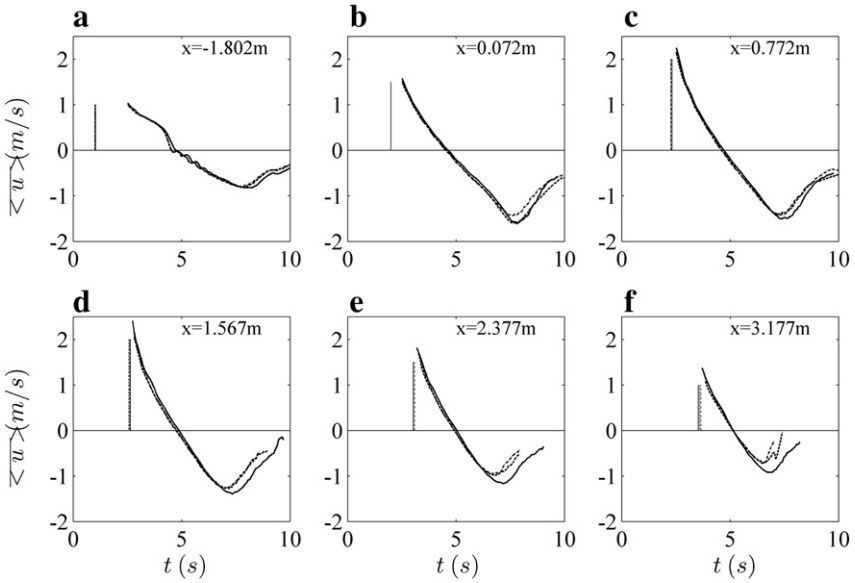

Fig. 12. Depth-averaged, bed-parallel velocity time-series at all six measurement locations for the 1.3 mm sand-rough (-), the 5.4 mm gravel-rough (--) and the 8.4 mm gravel-rough (-.-.) beaches; vertical lines indicate times of bore arrival.

measurement explains why maximum uprush velocity at $x = 0.072$ m appears to be lower than the maximum uprush velocity at locations higher up the beach. The flow accelerates in the backwash until it reaches a maximum backwash velocity when the retarding force due to bed friction balances the driving force due to the slope component of weight of water on the beach. Maximum uprush velocity is higher than maximum backwash velocity (although the actual maximum uprush velocity is not measured here because of the delay already described), the flow decelerates during the final stage of the backwash when the bed friction exceeds the driving force. Because of the shallow water depths, velocities are difficult to measure during the late stage of the backwash period. To the authors' knowledge only O'Donoghue et al. (2010) have previously obtained velocity measurements during this late stage, but their measurements are limited to backwash flow depth greater than 15 mm. The effect of beach roughness on the $\langle \overline{u} \rangle$ time-series is relatively small during uprush and for a significant part of the backwash. It becomes significant later in the backwash: for the rougher beaches, maximum backwash velocity is reached earlier and has lower magnitude.

3.3. Velocity profiles

Ensemble-averaged velocity profiles were generated from the simultaneous measurements of depth and velocity. Example profiles of bed-parallel velocity are shown for the 1.3 mm sand-rough beach in Fig. 13(a) and for the 8.4 mm gravel-rough beach in Fig. 13(b). The bottom-most measurement in each profile corresponds to $z \sim 3$ mm.

The velocity profiles are similar to the rough-beach profiles presented by O'Donoghue et al. (2010): the profiles have a typical "forward-leaning" shape during uprush, become close to depth-uniform at initial stages of the backwash, and become progressively more non-uniform as the velocity increases and depth decreases in the later stages of the backwash. Velocity gradients are highest close to the bed and, where the depth is large enough, approach near depth uniformity higher up the water column. Increasing bed roughness tends to increase the extent of the near-bed, high gradient flow; the effect is best seen by comparing the 1.3 mm sand-rough and the 8.4 mm gravel-rough profiles for $x = 0.772$ m. In the backwash, the flow depth decreases rapidly and the flow velocity increases (until it reaches the maximum backwash velocity). This results in bed-parallel velocity profiles with very steep near-bed gradients. For example, at the time of maximum backwash velocity on the 1.3 mm sand-rough beach at $x = 0.772$ m, the velocity increases from zero at the bed to -1.8 m/s at the surface within a depth of 25 mm.

Example profiles of bed-normal velocity are shown for $x = 0.772$ m for the three beaches in Fig. 14. The bed-normal velocities are close to zero for most of the swash event with the exception of the time just after bore arrival and at the late stage of the backwash, just before the time of maximum bed-parallel velocity. The short-lived, positive (upward) vertical velocities seen soon after bore arrival are likely due to the effect of the plunging wave: the resulting clockwise rotation (Miller, 1968; Petti and Longo, 2001) causes the fast fluid close to the free surface to hit the bed and move initially stagnant fluid forward and upward. In the backwash there is a tendency towards negative bed-normal velocity close to the bed. The reason for these negative velocities is unclear, but might be the local effect caused by the thin gap in bed roughness created to allow the light sheet to penetrate into the flow.

3.4. Turbulent kinetic energy and Reynolds stress

O'Donoghue et al. (2010) presented turbulent kinetic energy results for their smooth and rough beaches, but were limited by measuring one component of velocity (u) only. The present measurements include bed-normal velocities and so allow a fuller assessment of the flow turbulence. Fig. 15 presents profiles of turbulent kinetic energy, $TKE = \overline{u'u'} + \overline{w'w'}$ (where prime denotes a fluctuation, e.g. $u' = u - \bar{u}$, and overbar denotes ensemble-average), at selected times for three cross-shore locations ($x = 0.072$, 0.772 and 1.567 m) for the 1.3 mm sand-rough beach (Fig. 15a) and the 8.4 mm gravel-rough beach (Fig. 15b). Each panel shows the TKE profile at times corresponding to selected values of the depth-averaged velocity (indicated in the panel) for uprush and backwash. Note that the same depth-averaged velocity can occur twice in the backwash: once during backwash prior to the time of maximum backwash velocity and again during the late stage of backwash (see Fig. 12). Consider first the results for the 1.3 mm sand-rough beach in Fig. 15a. Close to the initial shoreline location ($x = 0.072$ m) and soon after bore arrival, *TKE* is relatively high and approximately constant throughout the flow column until just above the bed. This turbulent kinetic energy is generated by the wave collapse and is

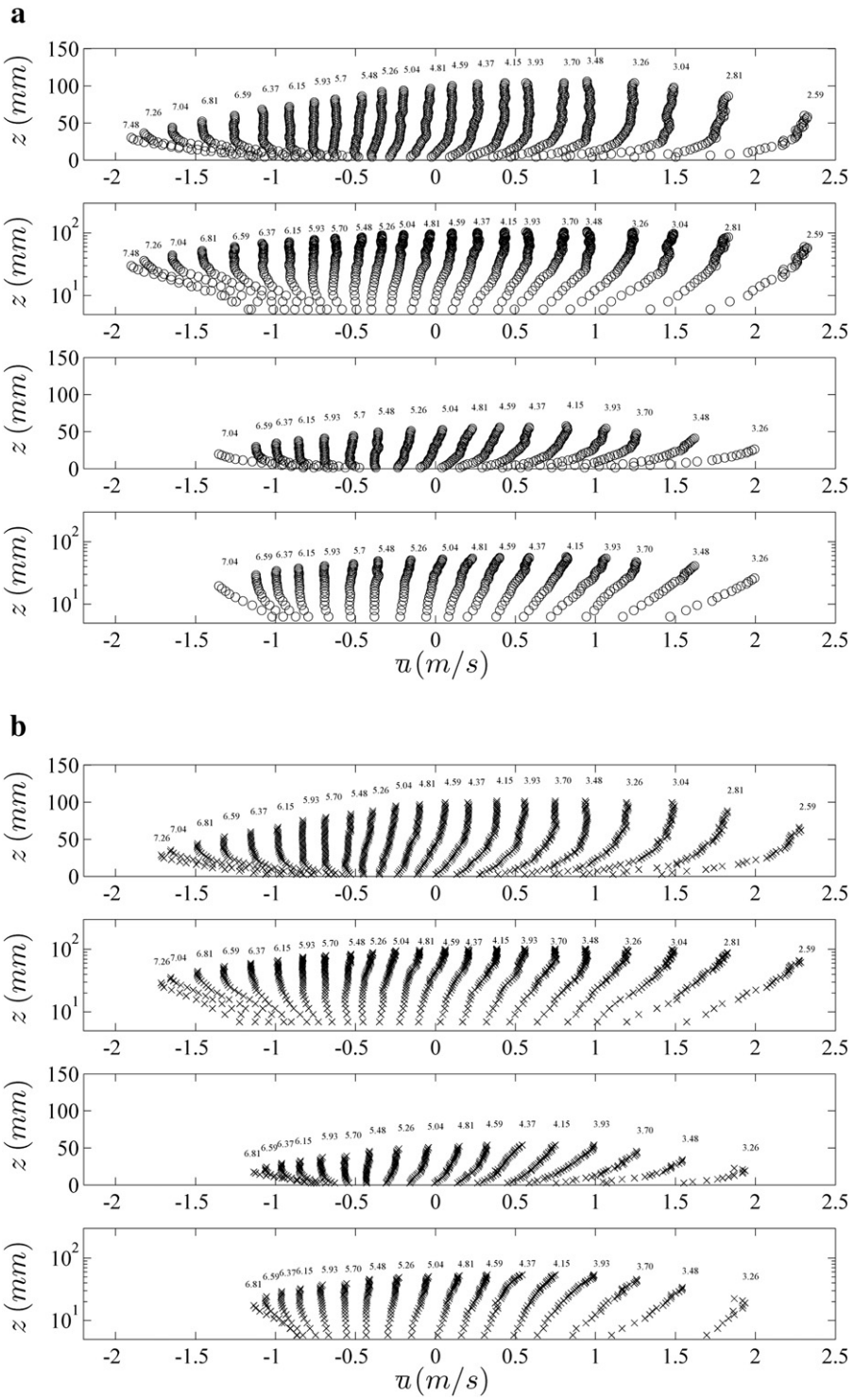

Fig. 13. (a). Ensemble-averaged, bed-parallel velocity profiles at $x = 0.772$ m for $t = 2.67$ s to 7.56 s (top 2 plots) and at $x = 2.377$ m for $t = 3.26$ s to 7.04 s (bottom 2 plots) for the 1.3 mm sand-rough beach; number above each profile is the time. (b). Ensemble-averaged, bed-parallel velocity profiles at $x = 0.772$ m for $t = 2.67$ s to 7.56 s (top 2 plots) and at $x = 2.377$ m for $t = 3.26$ s to 7.04 s (bottom 2 plots) for the 8.4 mm gravel-rough beach; number above each profile is the time.

transported with the flow onto the beach. The turbulent kinetic energy decays once the bore front has passed the measurement location and this trend persists over the upper section of the water column during the remainder of the uprush. Near the bed, high velocity gradients and intense shearing generate turbulence, so very soon after bore arrival the *TKE* profiles show a peak close to the bed. At later stages of the uprush, advected turbulence from lower locations is transported upwards and the peak in the *TKE* profile moves slightly away from the bed. At the same time the flow decelerates, thus decreasing *TKE* production and enhancing dissipation, so that the bed-generated *TKE* never reaches very high into the water column. By the end of the uprush most of the bore-generated turbulence has dissipated. The flow accelerates following flow reversal, creating high velocity gradients at the bed, developing the boundary layer and generating near-bed turbulence. These processes take time with the result that TKE is much lower than for the uprush (for the same depth-averaged velocity), and reaches significant levels only by the final stages of the backwash. Bore-generated turbulence dissipates

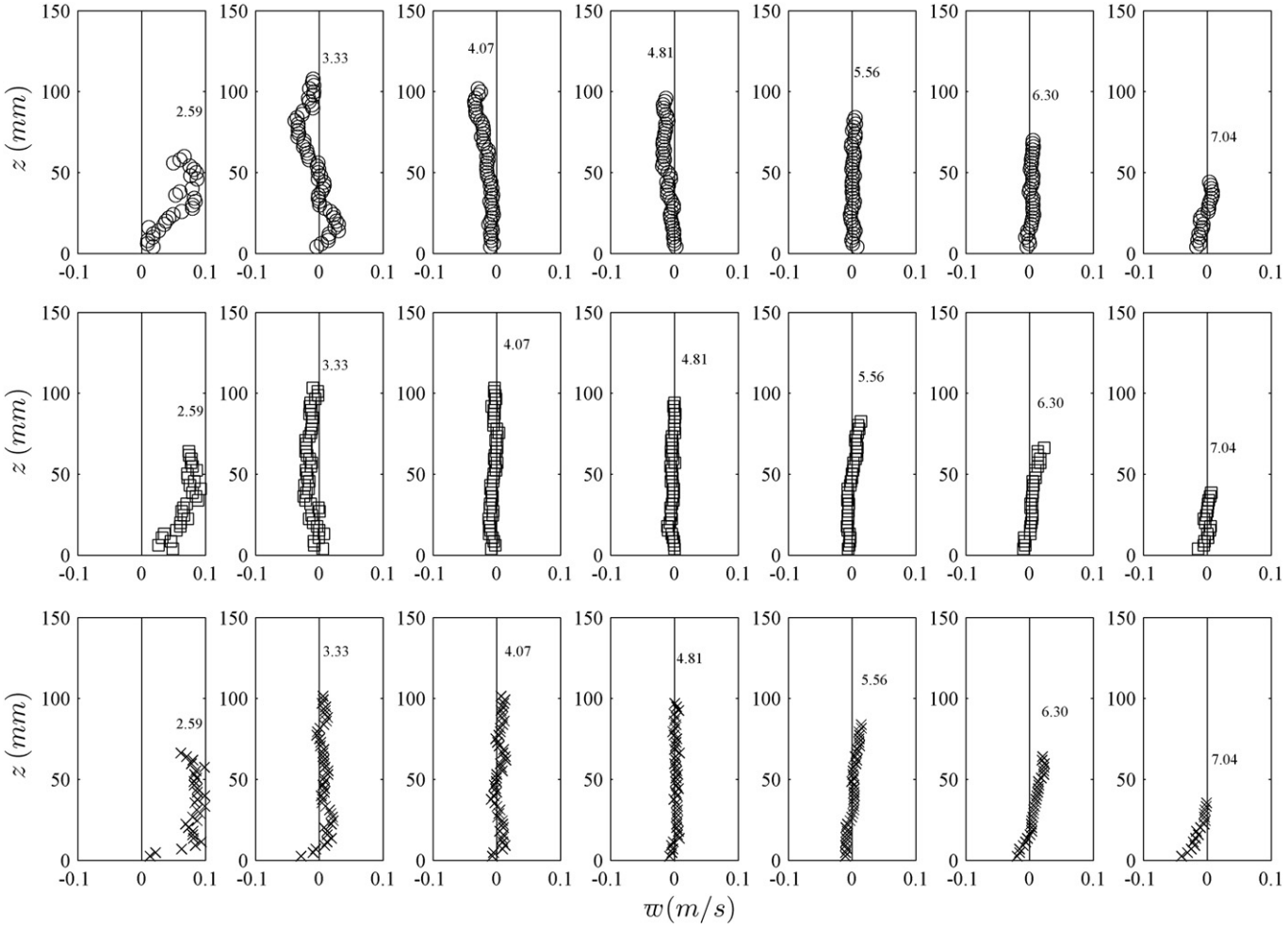

Fig. 14. Ensemble-averaged, bed-normal velocity profiles at $x = 0.772$ m and $t = 2.59$ s to 7.04 s for the 1.3 mm sand-rough beach (top), the 5.4 mm gravel-rough beach (middle) and the 8.4 mm gravel-rough beaches (bottom); the time associated with each profile is indicated.

as the bore progresses up the beach. At the same time bed-generated turbulence from lower locations on the beach is advected shorewards. The net result is *TKE* profiles that are much less depth-uniform compared to the *TKE* profiles at $x = 0.072$ m. For the 8.4 mm gravel-rough beach, Fig. 15b, *TKE* production and dissipation undergo similar behaviour over the swash cycle as for the 1.3 mm sand-rough beach. As expected, the incoming bore-generated turbulence is approximately similar for the two beaches, but bed-generated turbulence is higher for the rougher 8.4 mm beach. The results presented in Fig. 15 echo those of O'Donoghue et al. (2010) who presented *TKE* profiles based solely on bed-parallel velocity measurements and for somewhat lower depth-averaged velocities (0.8 m/s or less).

Fig. 16 presents time-series of depth-averaged turbulent kinetic energy, $\langle TKE \rangle$, for the five measurement locations on the 1.3 mm sand-rough and the 8.4 mm gravel-rough beaches. During the uprush $\langle TKE \rangle$ decreases due to dissipation of the bore-generated turbulence. Lower down the slope, $\langle TKE \rangle$ is slightly higher for the 8.4 mm gravel beach because of the higher production of bed-generated turbulence. Higher up the slope, this difference between the TKE appears to all but disappear, however this is related to the later bore arrival at this location on the rougher slope. The decrease in $\langle TKE \rangle$ resulting from the dissipation continues at all locations well past the time of $\langle \overline{u} \rangle$ reversal which is in agreement with measurements of Sou et al. (2010) on a smooth beach. Since the *TKE* transport at early stages of the backwash is still very low, the lowest level of $\langle TKE \rangle$ probably corresponds to a short period when dissipation is in balance with the bed-generated production. After this moment, $\langle TKE \rangle$ rapidly increases due to both higher production and higher transport resulting from the increasing flow velocities. At $x = 0.072$ m the increase continues until the time of maximum backwash velocity, while for locations further up the slope it continues for somewhat longer. At the final stage of backwash, $\langle TKE \rangle$ for the 8.4 mm gravel-rough beach is less than for the 1.3 mm sand-rough beach. This is related to the higher maximum backwash velocities in the latter case. Field estimates of *TKE* based on the root mean square of the vertical velocity by Hughes et al. (2007) showed that the mean turbulence intensity was higher during the uprush than the backwash, which is consistent with the results presented in Fig. 16.

In a similar manner to Fig. 15 for the *TKE* profiles, Fig. 17 presents profiles of Reynolds stress, $-\overline{u'w'}$, for three of the five measurement locations on the 1.3 mm sand-rough (Fig. 17a) and the 8.4 mm gravel-rough (Fig. 17b) beaches. After bore arrival at $x = 0.072$ m, Reynolds stress is non-zero near the free surface. This is probably the signature of the free surface turbulence remaining after the passage of the bore front; it diminishes further up the beach as expected. Generally the $-\overline{u'w'}$ profiles are consistent with the bed-parallel velocity profiles, with increasing stress nearer the bed where velocity gradients are steepest. The $-\overline{u'w'}$ profiles are similar to the *TKE* profiles shown in Fig. 15, except that the incoming turbulence comes with the shear stress close to zero. During uprush the bed-generated peak in turbulent shear stress moves higher into the flow column, indicating bed-normal transport of turbulent momentum and the associated development of the boundary layer. The

magnitude of $-\overline{u'w'}$ decreases as the flow decelerates and the near-bed velocity gradients become lower. Close to flow reversal the upper, more energetic part of the flow continues to move shoreward whereas the slower fluid close to the bed changes direction somewhat earlier. As a result, the Reynolds stress first changes sign near the bed. The change in the sign of $-\overline{u'w'}$ near the bed lags behind the change in the near-bed velocity direction by 0.6 s at the higher end of the beach and 0.9 s at the lower end. The delay is caused by the time it takes to generate turbulence at the bed level, and transport it in the bed-normal direction to the level of the lowest measurement point. This agrees with results from studies of unsteady flow generated by accelerating fluid in a pipe (He and Jackson, 2000; He et al., 2008) or by suddenly changing bed roughness (Chen and Chiew, 2003), where it was found that transfer of turbulence in the wall-normal direction is slower than other transfer processes resulting from flow unsteadiness or flow non-uniformity. In the early stages of the backwash $-\overline{u'w'}$ is therefore much lower than in the uprush, for the same velocity. However, at later stages of the backwash, $-\overline{u'w'}$ values close to the bed are similar to the uprush values. By this time the turbulent shear stress has been transported throughout the whole (rapidly decreasing) flow depth.

3.5. Bed shear stress

The detailed measurements of velocity offer the possibility, in principle, to estimate indirectly the intra-swash bed shear stress using a number of different methods: (i) application of momentum balance to a control volume; (ii) logarithmic profile fitting to the measured velocity profiles; (iii) from the near-bed peak in the turbulent shear stress; and (iv) relating the shear velocity to the turbulent kinetic energy dissipation rate obtained using the second order structure function. Of these methods, only momentum balance is strictly applicable to unsteady flow; each of the other three is based on principles that apply to steady flow and hence assume that local turbulent production equals local turbulence dissipation. At the same time, practical considerations can limit the applicability of a particular method. Kikkert et al. (2009) assessed the theoretical and practical viability of applying the different methods in the present context and showed that, because the second order structure function assumes homogeneous and isotropic turbulence, bed shear stress estimates based on turbulent kinetic energy dissipation rate could only be determined at times around flow reversal, when bed shear stress values are very low. For this reason only methods (i) to (iii) are considered further here.

For the momentum balance method, the individual terms of the Reynolds-Averaged Depth-Integrated Navier Stokes equations were evaluated using control volumes within the PIV field of view. The length of the control volume therefore decreased from approximately 100 mm for the location closest to the toe of the beach to 50 mm for the location furthest up the slope. The accuracy of the estimates increased when the height of the control volume was limited to approximately 30 mm. The log-law was applied in the same way as O'Donoghue et al. (2010), fitting to the six velocity measurements immediately above the bed and only accepting profiles with a 0.95 correlation between data and fit. This criterion eliminated velocity profiles close to the time of flow reversal: flow near the bed changes

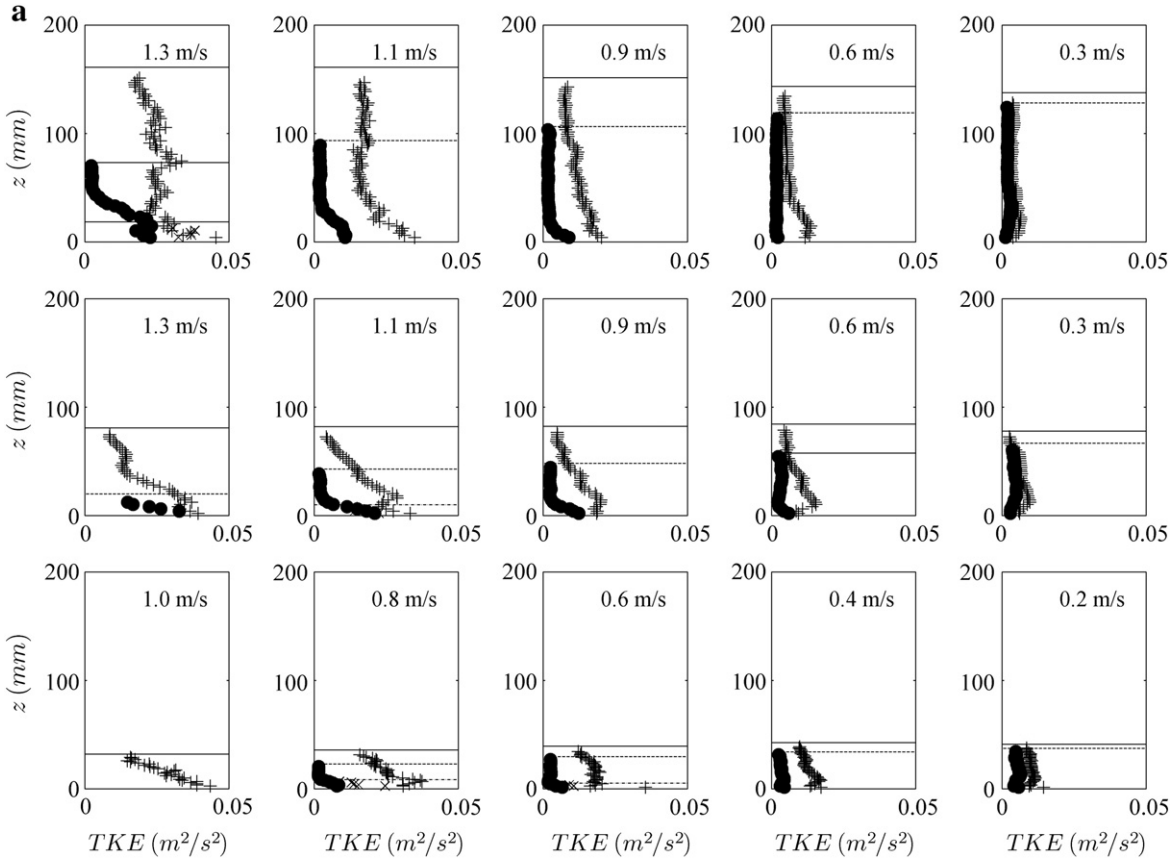

Fig. 15. a. Profiles of *TKE* corresponding to selected magnitudes of depth-averaged velocity during uprush (+), during backwash before time of maximum backwash velocity (●) and during late backwash (x). Horizontal lines indicate corresponding measured water depths during uprush (-), during backwash before time of maximum backwash velocity (--) and during late backwash (-.-.). Results are shown for the 1.3 mm sand-rough beach at $x = 0.072$ m (top panel), $x = 0.772$ m (middle) and $x = 1.567$ m (bottom). b. TKE profiles for the 8.4 mm gravel-rough beach. See caption Fig. 15a for details.

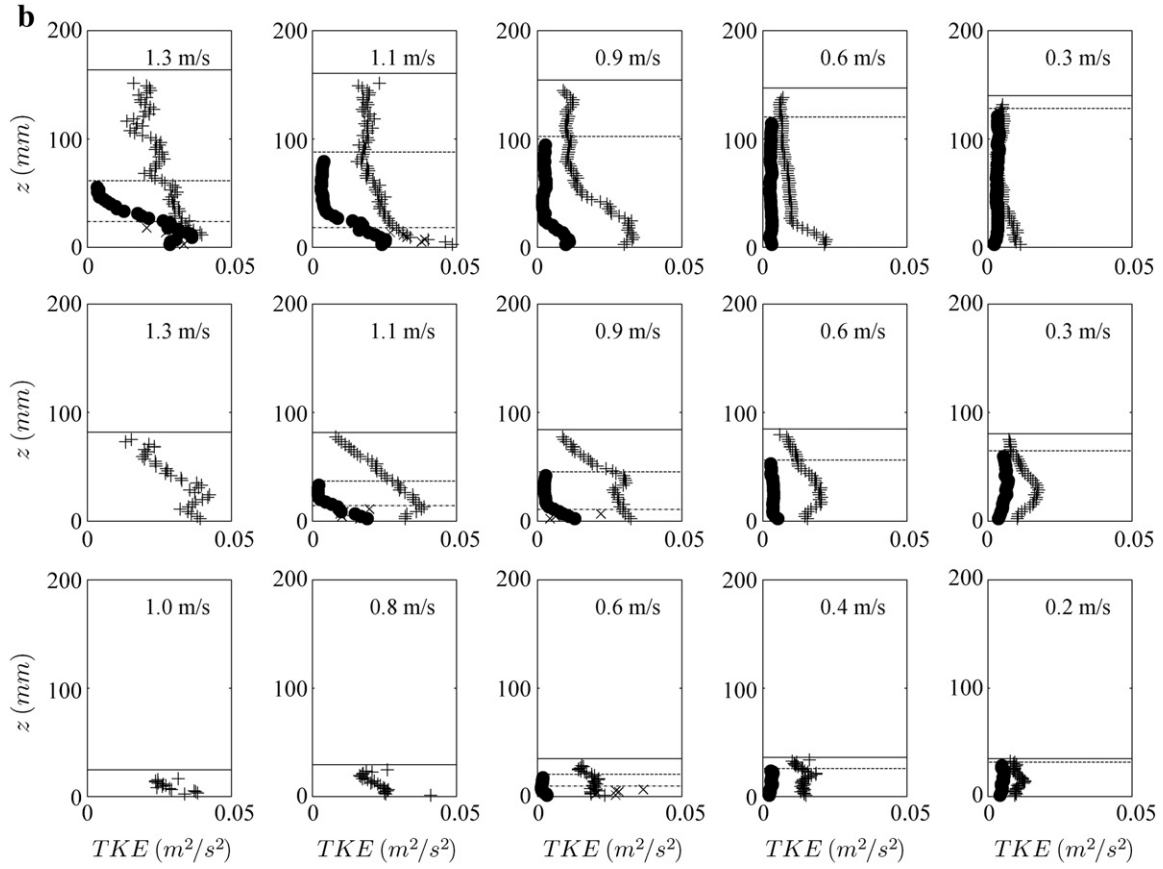

Fig.15 (*continued*).

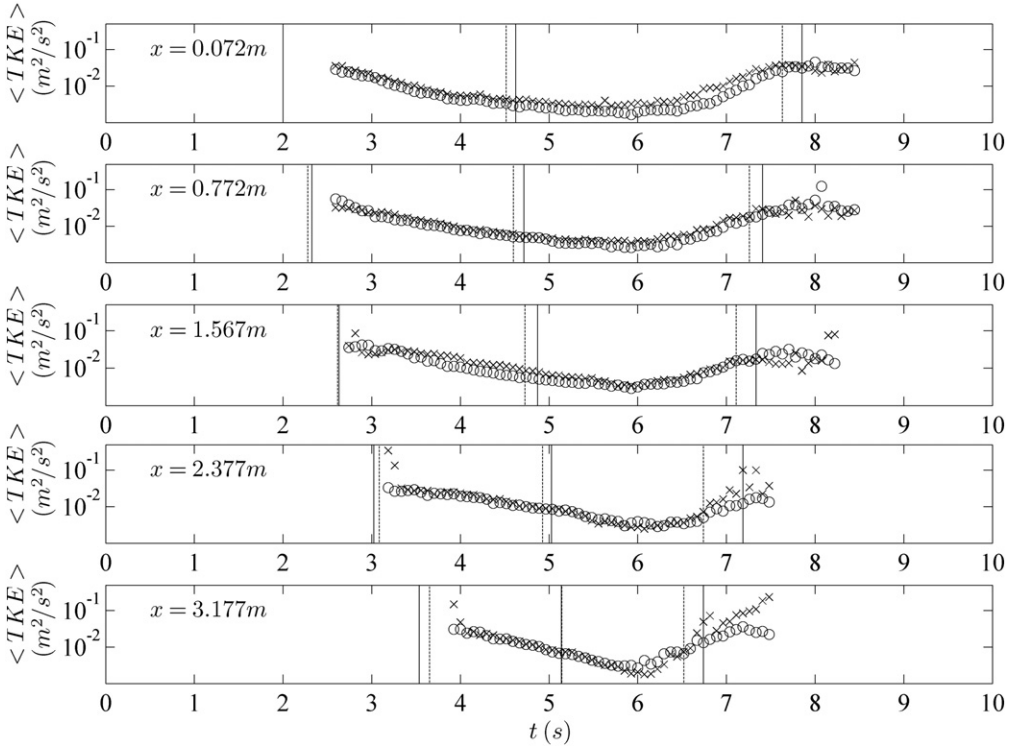

Fig. 16. Time-series of depth-averaged *TKE* at the 5 measurement locations on the 1.3 mm sand-rough beach (o) and the 8.4 mm gravel-rough beach (x); vertical lines correspond to time of bore arrival, time of depth-averaged flow reversal and time of maximum backwash velocity for 1.3 mm sand-rough beach (-) and 8.4 mm gravel-rough beach (--).

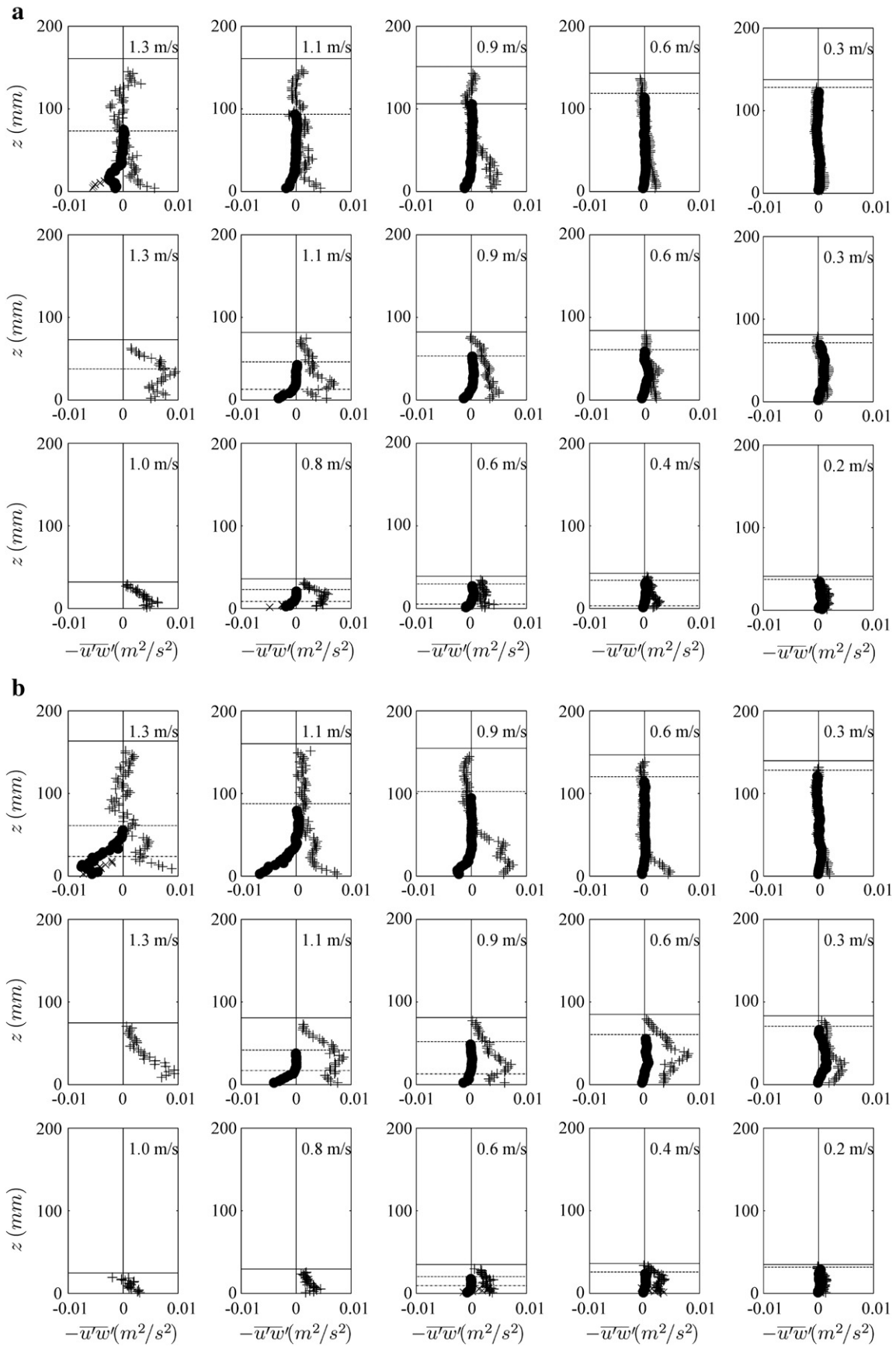

Fig. 17. a. Profiles of Reynolds stress corresponding to selected magnitudes of depth-averaged velocity during uprush (+), during backwash before time of maximum backwash velocity (●) and during late backwash (x). Horizontal lines indicate corresponding measured water depths during uprush (-), during backwash before time of maximum backwash velocity (--)and during late backwash (-.-.). Results are shown for the 1.3 mm sand-rough beach at $x = 0.072$ m (top panel), $x = 0.772$ m (middle) and $x = 1.567$ m (bottom). b. Profiles for Reynolds stress for the 8.4 mm gravel-rough beach. See caption Fig. 17a for details.

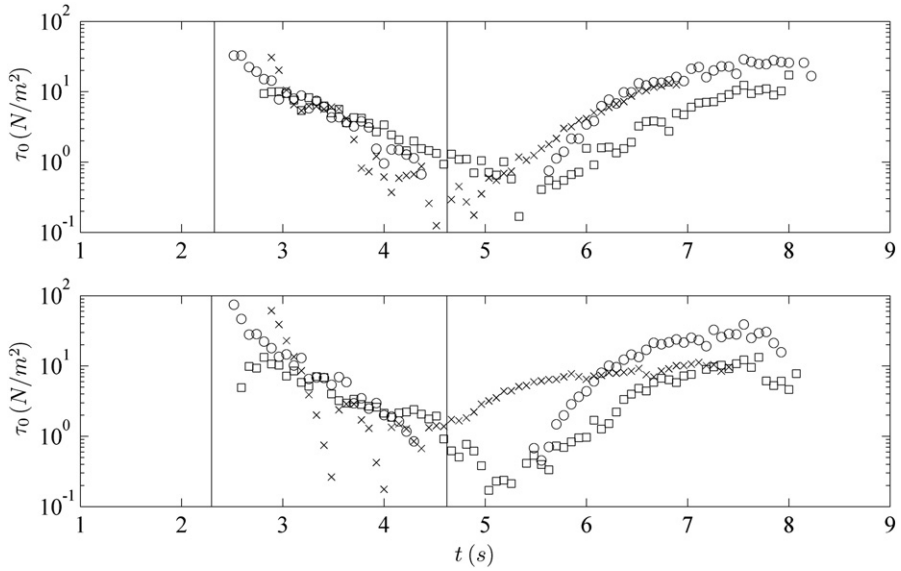

Fig. 18. Time-series of absolute bed shear stress obtained using the log law method (o), Reynolds stress method (□) and momentum balance method (x) at $x = 0.772$ m on the 1.3 mm sand-rough beach (upper panel) and the 5.4 mm gravel-rough beach (lower panel); vertical lines represent time of bore arrival and time of flow reversal.

direction before the flow in the rest of the profile, and in the backwash it takes some time for log layer to re-establish itself. The Reynolds stress method was applied by extrapolating the lower part of the Reynolds stress profile down to 2 mm above the bed (approximately the height of the measurement closest to the bed).

Fig. 18 presents typical bed shear stress time-series estimated from the velocity measurements via the momentum balance, log-law and Reynolds stress methods. The example results shown are for $x = 0.772$ m on the 1.3 mm sand-rough and 5.4 mm gravel-rough beaches. The results from the 1.3 mm sand-rough beach show a good overall agreement between the momentum balance and the log law method. The agreement is poorer close to flow reversal, when the momentum balance method is least accurate because all balance terms are very small. The Reynolds stress method agrees with the other two methods in the uprush, but in the backwash it produces results that lag behind them by up to 1 s. This delay is likely due to the same reason as that causing the delay in near-bed turbulent shear stress relative to the near-bed velocity, since the near-bed velocity is closely related to the bed shear stress. For the gravel-rough beaches the accuracy of the measurements was not sufficient to obtain useful estimates from the momentum balance method (lower panel of Fig. 18). The limitation of the control volume size relative to the size of the sediments appears to have negatively affected the results. Therefore, even though the momentum balance method is better-founded theoretically than the log-law method, in the following we concentrate on bed shear stress results obtained using the log-law method. Another benefit of the log-law method is that it has been extensively used in the literature, making comparison of our results with previous results more straightforward.

Fig. 19 presents time-series of bed shear stress (obtained using the log-law method) for the five cross-shore measurement locations on the 1.3 mm sand-rough (Fig. 19a), the 5.4 mm gravel-rough (Fig. 19b) and the 8.4 mm gravel-rough (Fig. 19c) beaches. The time-series shown in Fig. 19 have a similar shape for the three different beaches and five different locations. The bed shear stress is highest at the start of the uprush, although the maximum bed shear stress has not been captured because of the gap in time between bore arrival and first measurements of the velocities. During uprush, the logarithm of shear stress decays at nearly constant rate. After the time of flow reversal (between 5 and 6 s), bed shear stress first increases very quickly, followed by a tendency to plateau as the depth-averaged backwash velocity reaches its maximum. For a given beach, the highest backwash bed shear stress occurs at the most seaward location where backwash velocities are also highest. There is some indication that the shear stress decreases towards the very end of the backwash as both velocity and depth become low, but the effect is not completely captured because the very small flow depths did not allow the logarithmic profile to be fitted to the measurement data. The magnitude and time-varying behaviour of the bed shear stress are in good agreement with previous results reported by Barnes et al. (2009), who measured swash bed shear stress directly using a shear plate. Comparison of the present results with those reported by O'Donoghue et al. (2010) shows consistently lower bed shear stresses in the present experiments, especially in the backwash. O'Donoghue et al. (2010) attributed the discrepancy between their measures of bed shear stress and those of Barnes et al. (2009) to the experimental difficulties in measuring high velocities combined with low depths in the backwash. In the present experiments these difficulties have been overcome by using the better PIV set-up and a non-intrusive depth measurement.

Swash models commonly predict bed shear stress using a simple quadratic resistance law ($\tau = c_f \rho U^2/2$, where ρ is the density and U a representative velocity) with constant friction factor, c_f. Friction factor time-series for the 1.3 mm sand-rough and 8.4 mm gravel-rough beaches are presented in Fig. 20, calculated from the measured instantaneous bed shear stresses and depth-averaged velocities. The general behaviour in c_f for the two beaches is very similar. During uprush the friction factors are approximately constant until close to flow reversal, when they start to increase. During the early stages of the backwash the friction factors are much lower. They first increase rapidly, then more gradually, and reach an approximately constant value that is somewhat higher than the near-constant value seen in the uprush. These results are consistent with Masselink and Hughes (1998) who obtained an average friction factor for swash events in the field of 0.01 and uprush friction factor estimates of 0.005–0.01 and backwash estimates of 0.01–0.03 by Puleo and Holland (2001) inferred from uprush and backwash trajectories. However, the current results seem to contradict previously-published results from the field (Conley and Griffen, 2004) and from the laboratory (Barnes et al., 2009; Cowen et al., 2003; Cox et al., 2000) that have tended to conclude that uprush friction factors are greater than backwash friction factors. But we note that previous laboratory results for c_f are not based on simultaneous measurements of shear stress and velocity

profile, as they are here, while the method used in the field to obtain uprush and backwash velocities only allowed estimates for the friction factor during the time of bore arrival and late in the backwash.

The magnitudes of the friction factors for the two beaches are very similar over the majority of the swash cycle. This may be somewhat surprising since one would expect higher friction factors for the rougher beach. (For reference, friction factors calculated assuming *steady* and *uniform* flow and evaluated from the measured depths and velocities, with equivalent roughness of 1.3 mm and 8.4 mm, are consistently higher for the rougher beach by approximately

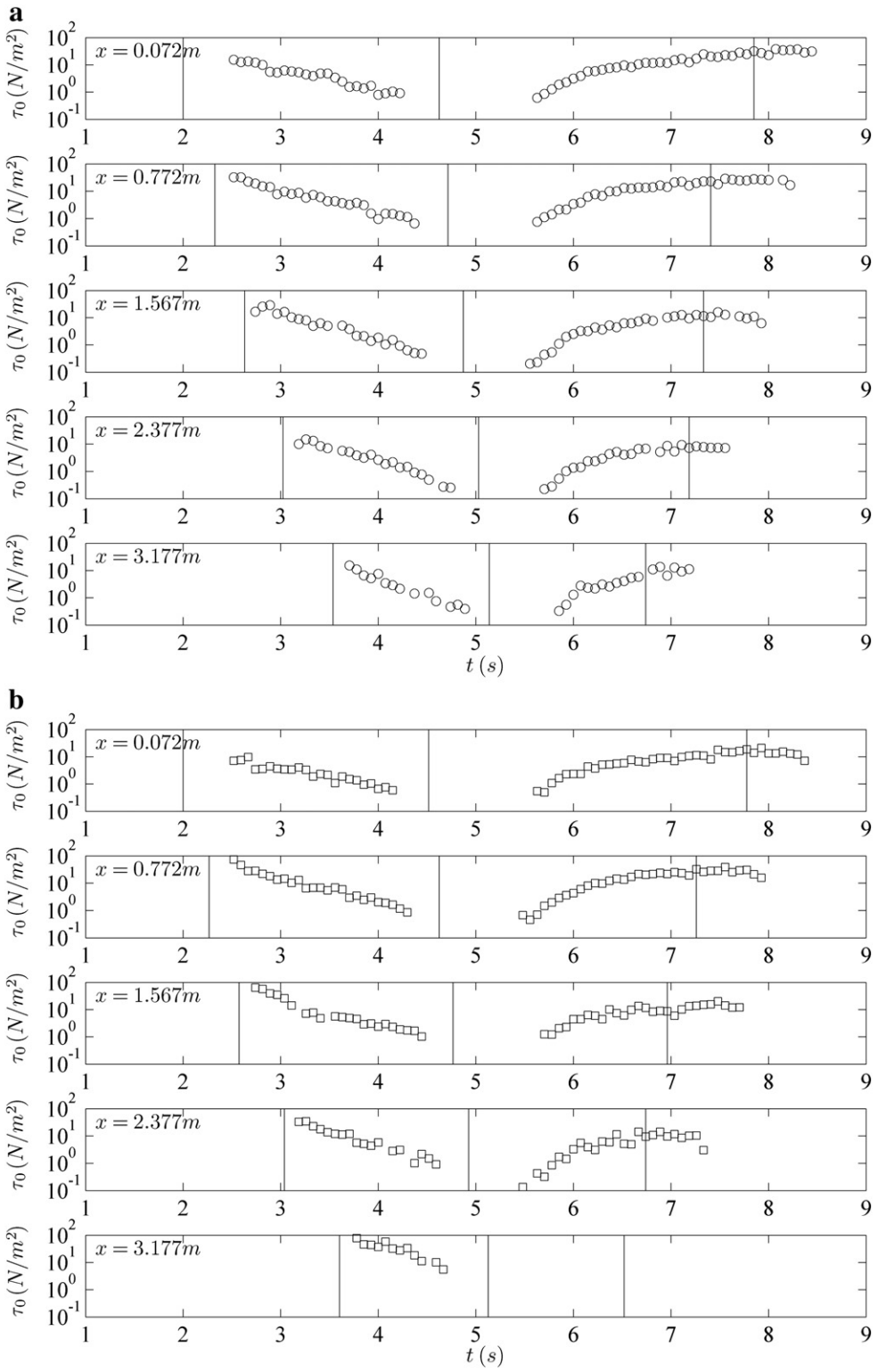

Fig. 19. a. Absolute bed-shear stress time-series for the five measurement locations on the 1.3 mm sand-rough beach obtained using the log law method. From left to right, vertical lines represent time of bore arrival, time of flow reversal and time of maximum backwash velocity. b. Absolute bed-shear stress time-series for the five measurement locations on the 5.4 mm gravel-rough beach obtained using the log law method. From left to right, vertical lines represent time of bore arrival, time of flow reversal and time of maximum backwash velocity. c. Absolute bed-shear stress time-series for the five measurement locations on the 8.4 mm gravel-rough beach obtained using the log law method. From left to right, vertical lines represent time of bore arrival, time of flow reversal and time of maximum backwash velocity.

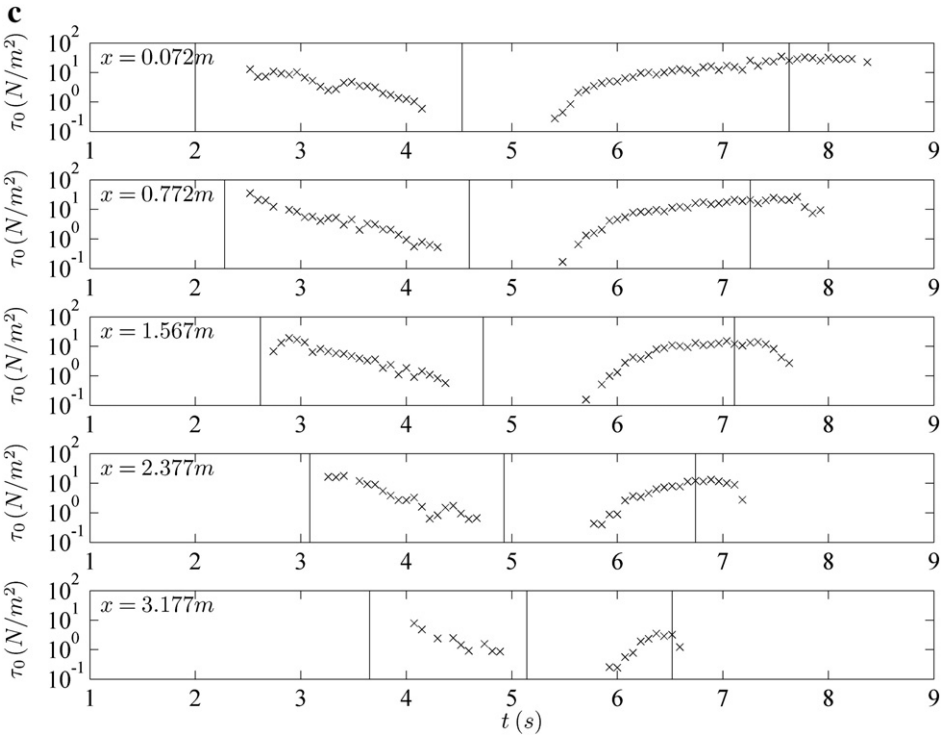

Fig.19 (*continued*).

50%.) The fact that the friction factors are not very different in the present experiments suggests that the high flow unsteadiness and non-uniformity of swash have significant influence on the bed shear stress for a given instantaneous velocity. The boundary layer development is likely to play a significant role and its effect can be observed in the results during the uprush. At $x = 0.072$ m the boundary layer has developed to only a limited extent, so the friction factors for the two beaches are very close. Further up the slope, beyond $x = 2.377$ m, the friction factors are higher for the coarser 8.4 mm beach. The increase in friction factor as flow reversal is approached is consistent with c_f behaviour in uniform, steady flow in that c_f is increasing with decreasing Reynolds number and higher relative roughness. In contrast, c_f behaviour during the early stage of the backwash is different from c_f behaviour in uniform, steady flow in that c_f is initially low, despite the Reynolds number being low and the relative roughness being high. Somewhat later, c_f values for the 8.4 mm beach catch up on the values for the 1.3 mm beach and then become higher than the 1.3 mm beach values, but only for locations higher up

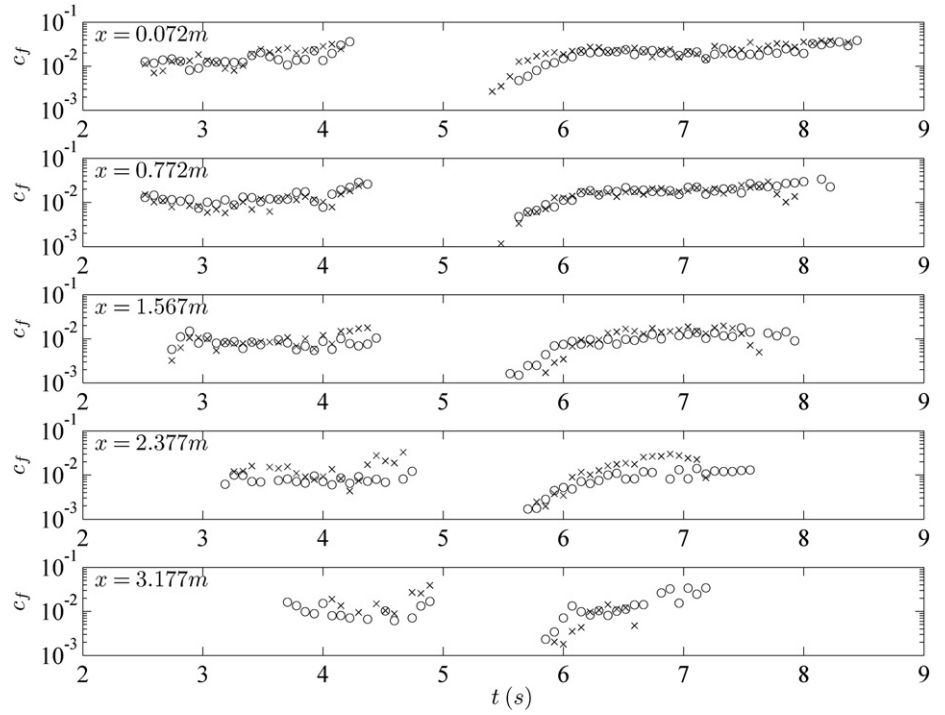

Fig. 20. Friction factor time-series at the five measurement locations for the 1.3 mm sand-rough beach (o) and the 8.4 mm gravel-rough beach (x).

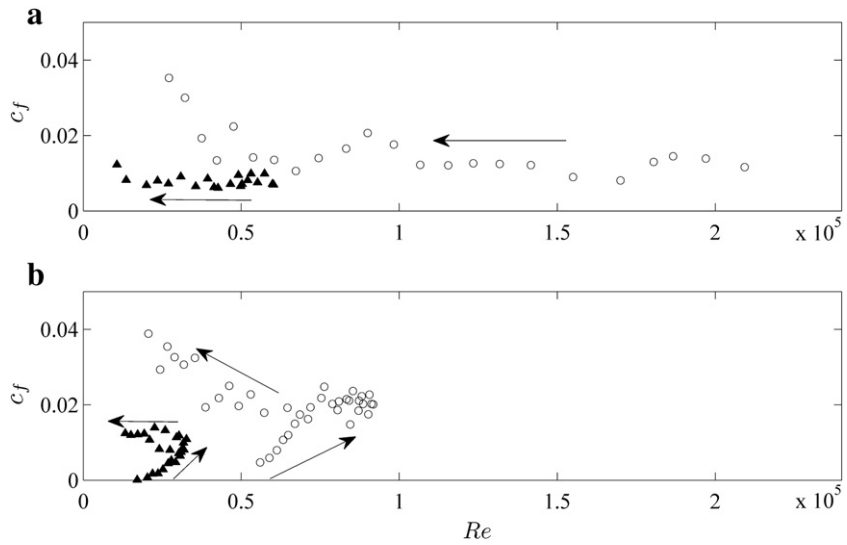

Fig. 21. Friction factor as a function of Re during uprush (top) and backwash (bottom) for $x = 0.072$ m (circles) and $x = 2.377$ m (triangles) on the 1.3 mm sand-rough beach; arrows indicate temporal sequence of data points.

the beach. At the two lowest locations on the beach c_f values are surprisingly similar during the backwash. This means that the boundary layer development is not sufficient to explain c_f behaviour throughout the whole swash cycle.

Fig. 21 shows the effect of beach location (hence available length for boundary layer development) on c_f, which is presented as a function of the Reynolds number ($\mathrm{Re} = \langle u \rangle \overline{h} / \nu$, where ν is the dynamic viscosity). c_f values corresponding to two locations on the 1.3 mm sand-rough beach are shown, one at a low beach position ($x = 0.072$ m) and one at a high beach position ($x = 2.377$ m). c_f is plotted separately for uprush and backwash and the temporal sequence of the data points is indicated by arrows. (In the uprush the sequence is from right to left because the Reynolds number is initially highest and decreases thereafter as velocity and depth decrease; in the backwash the sequence is left–right–left because *Re* first increases as flow accelerates, it reaches a maximum, and then decreases late in the backwash as the flow decelerates and becomes shallower.) There are two distinct periods when the friction factors behave differently from what would be expected for steady uniform flow. In the *late uprush*, friction factors at the lower end of the beach are much higher than for same Reynolds number at the upper end of the beach; friction factors are also higher than the corresponding steady uniform flow friction factors (calculated using the Colebrook–White equation with roughness equal to the sediment size). In the *early backwash*, friction factors at all locations are much lower than the corresponding steady uniform flow values, and they increase with increasing Reynolds number. Both effects can be explained by the boundary layer development. In the late uprush the behaviour typical for smooth wall persists until higher Reynolds numbers at the lower end of the beach, where the boundary layer has little time to develop. By the time the flow has reached the upper end of the beach the boundary layer has developed and the friction factors are closer to the corresponding steady uniform flow values. In the early backwash however, the development of the boundary layer occurs in accelerating flow which started from zero velocity. Low velocities, combined with the developing boundary layer, result in low values of friction factors.

4. Conclusions

A detailed experimental investigation of the hydrodynamics of large-scale, bore-driven swash on impermeable, rough beach slopes has been conducted. The experiments were carried out on three 1:10 impermeable, rough slopes with different surface roughness, adding substantially to the existing range of conditions for experiments of this type. Simultaneous measurements of depth and velocity using LIF and PIV respectively have resulted in better resolution of the hydrodynamics than previous studies. In particular, the new experiments resolve the backwash shoreline position and the late backwash period when depths are shallow and velocities are high, and they provide measures of bed-normal as well as bed-parallel velocities, enabling determination of the two-component turbulent kinetic energy and the Reynolds stress throughout the swash cycle. The following are the main conclusions from the analysis of the experimental data.

i. As expected, increased beach roughness reduces the shoreward reach of the swash lens and the maximum run-up.
ii. Roughness has limited effect on depth-averaged velocities during uprush. Differences in depth-averaged velocities between beaches of different roughness become significant only at the late stages of backwash, when flow over a rougher slope achieves lower (in absolute value) maximum velocity and starts to decelerate earlier than flow over a smoother slope. In contrast to previous studies, the late stages of backwash are well captured by the present measurements.
iii. The shapes of the velocity profiles are similar to those reported by O'Donoghue et al. (2010). Increasing bed roughness tends to increase the extent of the near-bed, high gradient flow.
iv. The present results for *TKE* based on two velocity components echo the *TKE* results presented by O'Donoghue et al. (2010) based on one velocity component (the streamwise component). The results show the signature of incoming turbulence, developing bottom boundary layer and rapid *TKE* dissipation as flow decelerates; dissipation continues during the early stages of backwash, followed by enhanced generation as the bottom boundary layer develops.
v. Reynolds shear stress profiles are consistent with the velocity profiles. As expected, the turbulent shear stress has a maximum close to the rough bed, where intense shearing generates turbulence. As the flow decelerates during uprush, the maximum shear stress is transported higher into the water column.
vi. Bed shear stresses evaluated using momentum balance and log-law show good overall agreement for the sand-rough beach; bed shear stresses evaluated via the Reynolds stress profiles agree reasonably well with the other methods in the

uprush, but show a lag in time compared to the other methods in the backwash; for the gravel-rough beaches, measurement accuracy was insufficient to obtain bed shear stress estimates via momentum balance.

vii. Estimates of uprush bed shear stress based on log profile fitting to the measured velocities agree well with direct shear plate measurements reported by Barnes et al. (2009), including for the late stages of the backwash.

viii. Friction factors are of the same order of magnitude $c_f \approx 0.01$ for all three rough beaches. Factors other than Reynolds number and relative roughness have significant influence on the bed shear stress for given instantaneous velocity. Friction factors in the backwash appear somewhat higher than in the uprush, a result that contradicts conclusions from previous studies.

ix. Fiction factors during the late stage of uprush and the early stage of backwash are affected by boundary layer development. At the lower end of the beach, friction factors during late uprush are higher than those for the corresponding steady uniform flow values; for all locations on the beach, friction factors during early backwash are lower than the corresponding steady uniform flow values.

x. The results for bed shear stress and friction factor show that the usual velocity squared parameterization of bed shear stress, with constant or variable friction factor (calculated using a steady uniform flow friction factor formula) cannot give accurate prediction of the bed shear stress. It seems that location on the beach and whether the flow is accelerating or decelerating have significant effect on the bed shear stress.

The experiments have yielded detailed data that can be used to test and develop advanced numerical models for bore-driven waves on rough slopes. The complete data are available on request to the authors.

Acknowledgements

The research was funded by the UK's Engineering and Physical Sciences Research Council (EPSRC) through awards EP/E011330/1 and EP/E010407/1 to the University of Aberdeen and the University of Nottingham respectively.

References

Aureli, F., Maranzoni, A., Mignosa, P., Ziveri, C., 2008. Dam-break flows: acquisition of experimental data through an imaging technique and 2D numerical modeling. Journal of Hydraulic Engineering 134 (8), 1089–1101.

Austin, M.J., Masselink, G., 2006. Observations of morphological change and sediment transport on a steep gravel beach. Marine Geology 229 (1–2), 59–77.

Barnes, M.P., O'Donoghue, T., Alsina, J.M., Baldock, T.E., 2009. Direct bed shear stress measurements in bore-driven swash. Coastal Engineering 56 (8), 853–867.

Chanson, H., 2004. Experimental study of flash flood surges down a rough sloping channel. Water Resources Research 40 (3), W033011–W0330112.

Chen, X., Chiew, Y., 2003. Response of velocity and turbulence to sudden change of bed roughness in open-channel flow. Journal of Hydraulic Engineering 129 (1), 35–43.

Conley, D.C., Griffen, J.G., 2004. Direct measurements of bed stress under swash in the field. Journal of Geophysical Research 109, C03050.

Cowen, E.A., Sou, I.M., Liu, P.L., Raubenheimer, B., 2003. Particle image velocimetry measurements within a laboratory-generated swash zone. Journal of Engineering Mechanics 129 (10), 1119–1129.

Cox, D.T., Hobensack, W., Sukumaran, A., 2000. Bottom stress in the inner surf and swash zone. Proceedings of the 27th International Conference on Coastal Engineering, 276, pp. 108–119.

Elfrink, B., Baldock, T., 2002. Hydrodynamics and sediment transport in the swash zone: a review and perspectives. Coastal Engineering 45 (3–4), 149–167.

Gedik, N., Irtem, E., Kabdasli, S., 2005. Laboratory investigation on tsunami run-up. Ocean Engineering 32 (5–6), 513–528.

He, S., Jackson, J.D., 2000. A study of turbulence under conditions of transient flow in a pipe. Journal of Fluid Mechanics 408, 1–38.

He, S., Ariyaratne, C., Vardy, A.E., 2008. A computational study of wall friction and turbulence dynamics in accelerating pipe flows. Computers and Fluids 37 (6), 674–689.

Hughes, M.G., 1992. Application of a non-linear shallow water theory to swash following bore collapse on a sandy beach. Journal of Coastal Research 8 (3), 562–578.

Hughes, M.G., Baldock, T.E., 2004. Eulerian flow velocities in the swash zone: field data and model predictions. Journal of Geophysical Research 109, C08009.

Hughes, M.G., Masselink, G., Brander, R.W., 1997. Flow velocity and sediment transport in the swash zone of a steep beach. Marine Geology 138 (1–2), 91–103.

Hughes, M.G., Aagaard, T., Baldock, T.E., 2007. Suspended sediment in the swash zone: heuristic analysis of spatial and temporal variations in concentration. Journal of Coastal Research 23 (6), 1345–1354.

Kikkert, G.A., Pokrajac, D., O'Donoghue, T., 2009. Bed-shear stress in bore-generated swash on steep beaches. Paper presented at 6th International Conference on Coastal Dynamics, Tokyo, Japan.

Masselink, G., Hughes, M., 1998. Field investigation of sediment transport in the swash zone. Continental Shelf Research 18 (10), 1179–1199.

Miller, R.L., 1968. Experimental determination of run-up of undular and fully developed bores. Journal of Geophysical Research 73 (14), 4497–4510.

O'Donoghue, T., Pokrajac, D., Hondebrink, L.J., 2010. Laboratory and numerical study of dambreak-generated swash on impermeable slopes. Coastal Engineering 57 (5), 513–530.

Petti, M., Longo, S., 2001. Turbulence experiments in the swash zone. Coastal Engineering 43 (1), 1–24.

Puleo, J.A., Holland, K.T., 2001. Estimating swash zone friction coefficients on a sandy beach. Coastal Engineering 43, 24–40.

Puleo, J.A., Beach, R.A., Holman, R.A., Allen, J.S., 2000. Swash zone sediment suspension and transport and the importance of bore-generated turbulence. Journal of Geophysical Research 105 (C7), 17021–17044.

Shin, S., Cox, D., 2006. Laboratory observations of inner surf and swash-zone hydrodynamics on a steep slope. Continental Shelf Research 26 (5), 561–573.

Sou, I.M., Cowen, E.A., Liu, P.L., 2010. Evolution of the turbulence structure in the surf and swash zones. Journal of Fluid Mechanics 644, 193–216.

Sue, L., Nokes, R., Walter, R., 2006. Experimental modeling of tsunami generated by underwater landslides. Science of Tsunami Hazards 24 (4), 267–287.

Yeh, H.H., 1991. Tsunami bore runup. Natural Hazards 4 (2–3), 209–220.

Zech, Y., Soares-Frazão, S., Spinewine, B., Le Grelle, N., 2008. Dam-break induced sediment movement: experimental approaches and numerical modelling. Journal of Hydraulic Research 46 (2), 176–190.